Analysis of temporal separation through time-localized resolvent forcing and response modes

Micah Nishimoto[1], Min-Lin Tsai[2], H. Jane Bae[1] and Scott T. M. Dawson[2]

[1]Graduate Aerospace Laboratories, California Institute of Technology, Pasadena, CA, USA 91125

[2] Department of Mechanical, Materials, and Aerospace Engineering, Illinois Institute of Technology, Chicago, IL, USA

E-mail: mnishimo@caltech.edu, mtsai6@illinoistech.edu

Abstract. We investigate transient separation using turbulent Couette–Poiseuille (C-P) flow subjected to a sudden strong adverse pressure gradient (APG). Using a space-time resolvent framework constructed around the time-varying mean flow, we identify spatiotemporal forcing modes that are optimally amplified by the linearized Navier-Stokes operator, along with their corresponding response modes. Our analysis shows that different streamwise and spanwise scales are preferentially amplified in different temporal regions of the flow, with the trends consistent with statistics computed from direct numerical simulations. Time-localized resolvent modes also indicate the causal relationship between forcing and response modes, characterized by a temporal delay between their amplitude peaks. Time-windowed analysis of the resolvent operator reveals how linear amplification evolves over time, linking distinct time scales to different spatial scales throughout the separation event. We further show that a reduced-order model featuring a small number of space-time resolvent modes can be used as a simplified model for unsteady separation events, with a three-mode model capable of accurately capturing the extent of flow reversal over time at a near-wall location.

1 Motivation

Flow separation is a ubiquitous phenomena in aerodynamic flows, often associated with adverse effects such as loss of lift, increase in drag, and noise generation [1, 2]. Separation typically occurs in turbulent flow in the presence of an adverse pressure gradient (APG) or a geometric feature that inhibits the boundary-layer attachment. Recent works have emphasized the dynamics and coherent structures of separation events in spatially-evolving, statistically stationary flow configurations [3, 4]. Even in such canonical settings, separation remains a complex process involving a broad range of spatial and temporal scales.

To interpret the dynamics underlying such interactions, growing attention has been placed on linear amplification mechanisms as drivers of separation-related motion in the near-wall region. Resolvent analysis provides a powerful framework for quantifying these mechanisms by linearizing the Navier–Stokes equations around a turbulent mean and treating the nonlinear terms as an external forcing [5, 6]. The resolvent operator thereby captures how specific forcing structures are amplified by the linear dynamics. Variants of resolvent analysis have been used to study stationary separated flow events, in configurations ranging from canonical to complex. For example, Soria, *et al.* [7] show how resolvent analysis can identify

nonlinear forcing and response modes in a self-similar turbulent boundary layer at the verge of separation across different length and frequency scales. Similarly, spatial regions sensitive to optimal flow perturbations and its corresponding energy amplification mechanisms have been identified in separated flows around airfoils using resolvent analysis, providing insight on the behavior of laminar separation bubbles [1, 4, 8]. The above studies indicate that resolvent analysis can be a valuable tool for understanding, modeling, and prediction of stationary separation events.

However, transient separation events in turbulent boundary layers pose additional challenges. These events are intermittent, often manifesting as extreme excursions from the mean state [9–11]. On smooth surfaces without geometric confinement, the location and evolution of the separation point can vary widely in space and time [10, 12]. Moreover, in highly complex turbulent flows, isolating the specific flow physics leading to separation onset is nontrivial [3, 13]. Consequently, conventional modal analyses based on stationary or periodic assumptions fail to isolate the mechanisms governing these rapid transitions.

To address this limitation, we employ a time-localized extension of resolvent analysis [14, 15] that resolves the transient amplification mechanisms leading to separation. Using direct numerical simulations (DNS) of turbulent Couette–Poiseuille (C-P) flow subjected to both a streamwise APG and upper-wall motion [12, 16–18], we simulate the transition from attached to separated wall-bounded turbulent flow through a sudden change of the mean APG. The characteristics of the flow at these conditions are similar to a fully separated boundary layer, leading to a lower surface boundary exhibiting separation events that are intermittent in both space and time; hence, the dynamics of this flow configuration is akin to a transient turbulent separation bubble. Important to note is the presence of reverse flow events within transient separation. Regions of critical points of zero velocity and rare backflow events of negative streamwise velocity have been identified in DNS of stationary turbulent channel flows without APG environments [19, 20]; the presence of reverse flow events has been studied experimentally in turbulent boundary layers with and without a mean APG, where it was found that the reverse flow probability nearly doubles under the influence of the APG [21]. In a similar spirit, this study utilizes an explicitly time-dependent pressure gradient, where the number of reverse flow events is expected to increase in time.

We examine two complementary extensions of resolvent analysis for time-varying systems. The first approach involves analyzing the space-time resolvent operator directly, without assuming a form for the temporal functions. This approach identifies space-time forcing and response modes associated with maximum linear energy amplification. While this approach would reproduce Fourier modes in time given a stationary mean, it will generally not do so for nonstationary systems [14]. While not explored here, note that it is also possible to localize these structures through a modification of the usual energy-based optimization problem associated with resolvent analysis [14]. The second approach involves forming the resolvent operator using wavelet transforms rather than Fourier transforms in time. This preserves both frequency and time information and allows for identification of nonlinear forcing modes that are optimally amplified about a time-varying turbulent mean profile [15]. The use of wavelet transforms allows for time and frequency windows to be supplied in the construction of the resolvent operator. Localized forcing and response modes can subsequently be identified, illuminating the mechanisms associated with separation occurring at different frequency scales in the temporal regions confined to high and low-shear at the lower surface boundary.

The present work focuses on applying the methodologies developed in Refs. [14, 15] to study the dynamics of transient C-P flow. In particular, we utilize space-time and wavelet-based resolvent analysis in two contexts: (i) to identify cause-and-effect relationships between forcing and response dynamics during transient separation, and (ii) to construct reduced-order models based on a small number of space–time modes capable of reconstructing key features and statistics of near-wall separation. Comparisons with DNS statistics across spatial and temporal scales, along with utilization of metrics unique to C-P flows, provide new insight into the linear mechanisms governing unsteady separation in turbulent wall-bounded flows containing pressure gradients with arbitrary time dependence.

This proceeding is organized as follows.§ 2 describes the DNS of the transient turbulent C-P flow and mentions key statistics and their spatiotemporal trends. In § 3, we utilize the base flow from the DNS to obtain space-time resolvent modes in two different formulations; one constructs the resolvent operator in physical time (§ 3.1), while the other utilizes a wavelet basis to encode time and frequency information in the resulting modes (§ 3.2). The results are subsequently analyzed in § 4 via the lens of cause-and-effect, and in § 5 to model and visualize the evolution of reverse flow regions near the lower wall. Conclusions are presented in § 6.

2 Direct numerical simulation setup

We perform a series of DNS of incompressible turbulent C-P flow subjected to a sudden imposition of a strong APG. The calculation is initialized with a statistically stationary DNS of C-P flow representative of an attached APG turbulent boundary layer. At $t = 0$, the mean APG is suddenly increased such that the statistically stationary case will result in flow separation.

The simulations are performed by discretizing the incompressible Navier-Stokes equations with a second-order accurate centered finite difference scheme in space [22], with a third-order Runge-Kutta time advancement scheme [23], with a fractional step method to compute the pressure [24]. We note that quantities are nondimensionalized by the channel half-height h, the half upper-wall velocity $U_c = U_w/2$, and the density ρ. The size of the computational domain is $(L_x \times L_y \times L_z) = (6\pi \times 2 \times 3\pi)$, where $\boldsymbol{x} = (x, y, z)$ are the streamwise, wall-normal, and spanwise flow directions. The domain is discretized uniformly in the streamwise and spanwise directions with $N_x = N_z = 512$ points, and a Chebyshev grid with $N_y = 256$ is implemented in the wall-normal direction. Periodic boundary conditions are imposed in the streamwise and spanwise direction. The bottom wall is stationary and the top wall is moving at a constant velocity of $U_w = 2$.

The initial statistically stationary DNS is performed for C-P flow representative of attached wall-bounded turbulent flow by applying a mean streamwise pressure gradient $dP/dx = 0.003$. We note that the Couette Reynolds number $Re_c = U_c h/\nu = 2500$, where ν is the kinematic viscosity. The friction Reynolds number at the lower wall at this initial condition $Re_{\tau_0,\text{low}} = u_{\tau_0,\text{low}} h/\nu = 57.5$ and the upper-wall friction Reynolds number $Re_{\tau_0,\text{up}} = u_{\tau_0,\text{up}} h/\nu = 215$, where $u_{\tau_0,\text{up}}$ and $u_{\tau_0,\text{low}}$ are the initial friction velocities at the upper and lower wall, respectively. Furthermore, we note that the direction of dP/dx is chosen such that the lower wall experiences an APG, whereas the upper wall experiences a favorable pressure gradient (FPG). The mean APG is then suddenly increased to $dP/dx = 0.005$ at $t = 0$. An ensemble of 20 individual transient separation simulations are considered by initializing the simulations with various temporally uncorrelated statistically stationary C-P flow. The simulations are run for $t = 620$, which is 14.5 flow through times based on the initial friction velocity at the upper wall $u_{\tau_0,\text{up}}$ and channel half height. We note that the average wall shear stress at the bottom wall decreases in time, reaching a zero-crossing at $t = 465$, as seen in Figure 1.

We introduce the Reynolds decomposition of the velocity and pressure fields over a finite time window $\boldsymbol{u}(\boldsymbol{x}, t) = \boldsymbol{U}(y, t) + \boldsymbol{u}'(\boldsymbol{x}, t)$, $p(\boldsymbol{x}, t) = P(y, t) + p'(\boldsymbol{x}, t)$, where $\boldsymbol{U}(y, t) = [U(y, t), \boldsymbol{0}, \boldsymbol{0}]$ and $\boldsymbol{u}'(\boldsymbol{x}, t) = [u'(\boldsymbol{x}, t), v'(\boldsymbol{x}, t), w'(\boldsymbol{x}, t)]$ are the mean and fluctuating velocity components, and $P(y, t)$ and $p'(\boldsymbol{x}, t)$ are the mean and fluctuating pressure components. The mean and r.m.s. velocity profiles for the statistically stationary cases as well as the evolution of the transient case are given in Figure 1. This time-varying mean $U(y, t)$, obtained by averaging over x, z, and all ensembles for each y and t value, will be utilized to form the resolvent operators described in § 3. Note that in general, fully-converged time-varying mean states of temporally evolving flows are more difficult to obtain than means for statistically-stationary flows, since time-averaging is not permitted. For this flow, streamwise and spanwise homogeneity means that we achieve a converged mean state using a modest number of ensembles, within needing any additional filtering or time-windowing of the data. The addition and removal of ensemble members to the computation of the mean has little effect on the resolvent results. More generally, note that the sensitivity of resolvent analysis to mean uncertainty is an active area of research [25].

3 Space-time resolvent modes

The DNS yields a base flow $\boldsymbol{U}(y, t)$ that we will use to analyze linear energy amplification mechanisms in the transient turbulent C-P flow. Due to the transient nature of this flow, traditional resolvent analysis using Fourier transforms in time is not appropriate. Instead, we use generalized space-time resolvent analysis tools as described in [14, 15]. In space-time resolvent analysis, the incompressible Navier–Stokes equations are first linearized about the turbulent mean,

$$\frac{\partial \boldsymbol{u}'}{\partial t} + \boldsymbol{U}\cdot\nabla\boldsymbol{u}' + \boldsymbol{u}'\cdot\nabla\boldsymbol{U} + \nabla p' - \frac{1}{Re}\Delta\boldsymbol{u}' = \boldsymbol{f}', \qquad \nabla\cdot\boldsymbol{u}' = 0, \tag{1}$$

where $\boldsymbol{f}$ are the nonlinear terms and $Re = U_c h/\nu$. The equations are then Fourier transformed in the two homogeneous directions x and z giving the linear system

$$\begin{bmatrix} \boldsymbol{D}_t + \boldsymbol{L} & \widehat{\boldsymbol{\nabla}} \\ \widehat{\boldsymbol{\nabla}}^T & 0 \end{bmatrix} \begin{bmatrix} \boldsymbol{u}' \\ p' \end{bmatrix} = \begin{bmatrix} \boldsymbol{f}' \\ 0 \end{bmatrix}, \quad \boldsymbol{L} = \begin{bmatrix} ik_x U - \hat{\Delta}/Re & D_y U & 0 \\ 0 & ik_x U - \hat{\Delta}/Re & 0 \\ 0 & 0 & ik_x U - \hat{\Delta}/Re \end{bmatrix}, \tag{2}$$

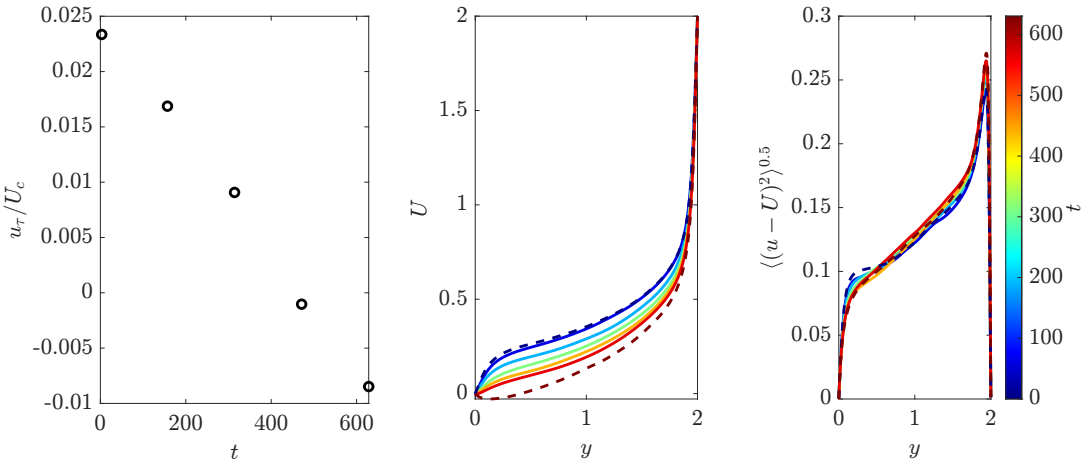

(a) (b) (c)

Figure 1: (a) Friction velocity at the lower wall u_τ evolving in time, plotted for $t = [3.14, 157, 314, 470, 620]$. (b) Evolution of mean streamwise velocity U for the DNS of the transient C-P flow with a sudden APG. Dashed lines indicate stationary mean streamwise velocity profiles for $dP/dx = 0.003$ (blue) and $dP/dx = 0.005$ (red). Solid lines indicate mean profile at $t = [3.14, 157, 314, 470, 620]$. (c) Evolution of the streamwise r.m.s. velocity $\langle(u-U)^2\rangle^{0.5}$ for the DNS of the transient C-P flow with a sudden APG, with the dashed and solid lines indicating the same flow states as in (b).

where $\hat{(\cdot)}$ represents Fourier-transformed quantities, $\boldsymbol{D}_t$ represents a first-order time derivative, $\widehat{\boldsymbol{\nabla}} = [ik_x, D_y, ik_z]^T$, and $\widehat{\Delta} = -(k_x^2 + k_z^2) + D_{yy}$. Here k_x and k_z are the wavenumbers in the x and z directions, respectively, and D_y and D_{yy} are respectively the first and second derivatives in y.

In the subsequent subsections, we introduce two types of space-time resolvent formulations under the framework designed for this time-varying base flow. In both cases, the wall-normal coordinate is discretized on a Chebyshev collocation grid $\{y_j\}_{j=1}^{N_y}$, and the wall-normal differentiation operators D_y and D_{yy} are Chebyshev differentiation matrices.

3.1 Direct space-time resolvent analysis

In direct space-time resolvent analysis, the complete temporal differential operator is retained and the space-time resolvent operator follows directly from equation (2) as

$$\boldsymbol{\mathcal{H}}_t = \begin{bmatrix} \boldsymbol{D}_t + \boldsymbol{L} & \widehat{\boldsymbol{\nabla}} \\ \widehat{\boldsymbol{\nabla}}^T & 0 \end{bmatrix}^{-1}. \tag{3}$$

The singular value decomposition (SVD) of $\boldsymbol{\mathcal{H}}_t = \hat{\boldsymbol{\Psi}}\hat{\Sigma}\hat{\boldsymbol{\Phi}}^*$ is performed to identify the right and left singular vectors $\hat{\boldsymbol{\Phi}}_i = [\hat{\phi_u}, \hat{\phi_v}, \hat{\phi_w}, \boldsymbol{0}]_i^T$ and $\hat{\boldsymbol{\Psi}}_i = [\hat{\psi_u}, \hat{\psi_v}, \hat{\psi_w}, \hat{\psi_p}]_i^T$, with the superscript $*$ indicating the adjoint. Following Ballouz, *et al.* [26, 27], the perturbation kinetic energy norm is utilized to calculate the inner product in the SVD. Note that unlike standard resolvent analysis, these singular vectors are functions of both space and time. The leading right singular vectors reveal the inputs that are most optimally amplified by the time-varying resolvent operator, with the left singular vectors giving the (normalized) response of the system to these forcings to the system. The singular values $\hat{\sigma}_i$ represent the corresponding amplification factor between the forcing and response.

3.2 Wavelet-based resolvent modes

In wavelet-based resolvent analysis, rather than retaining the complete temporal differential operator, we use a wavelet transformation in time [15, 28–30]. Thus, the equations in (2) are additionally transformed in time using a wavelet basis such that

$$\boldsymbol{\mathcal{H}}_w\mathcal{B} = \begin{bmatrix} \widetilde{\boldsymbol{D}}_t + \boldsymbol{L} & \widehat{\boldsymbol{\nabla}} \\ \widehat{\boldsymbol{\nabla}}^T & 0 \end{bmatrix}^{-1} \mathcal{B}, \tag{4}$$

where $\boldsymbol{\mathcal{H}}_w$ is the wavelet-based resolvent operator, $\widetilde{\boldsymbol{D}}_t$ is the discrete wavelet-transformed time derivative, and $\mathcal{B}$ is a windowing matrix. In the current study, the wavelet transform is given by a single-level, Daubechies 16-tap wavelet transform [28] with smooth-padding edge conditions to minimize the presence of numerical artifacts at the temporal extrema [29, 30].

The use of wavelet transforms allows for time and frequency windows to be supplied in the construction of the resolvent operator. $\mathcal{B}$ windows the forcing modes in time and frequency via restriction onto a wavelet with specified shift and scale, which correspond to frequency and time information, by setting specific columns corresponding to time and frequency regions outside of the regions of interest to zero [1, 26, 27]. This serves as a means to localize the resolvent operator to only consider the nonlinear mechanisms confined to a specific time and frequency band.

Subsequently, localized forcing and response modes can be identified via the SVD of $\boldsymbol{\mathcal{H}}_w\mathcal{B} = \widetilde{\boldsymbol{\Psi}}\widetilde{\Sigma}\widetilde{\boldsymbol{\Phi}}^*$, where $\widetilde{\boldsymbol{\Phi}}_i = [\widetilde{\phi_u}, \widetilde{\phi_v}, \widetilde{\phi_w}, \boldsymbol{0}]_i^T$ and $\widetilde{\boldsymbol{\Psi}}_i = [\widetilde{\psi_u}, \widetilde{\psi_v}, \widetilde{\psi_w}, \widetilde{\psi_p}]_i^T$, represent the windowed resolvent forcing and response modes. Similar to the direct space-time resolvent modes in § 3.1, these are spatiotemporal modes where the leading forcing modes describe the constrained forcing that is most optimally amplified by the wavelet-based resolvent operator. In turn, by constraining the forcing modes to specific time regions in the transient C-P flow, the corresponding modes illuminate the mechanisms associated with separation occurring at different frequency scales in confined temporal regions; the window provided by the definition of $\mathcal{B}$ and the use of a wavelet basis acts as an extension of the direct space-time formulation in § 3.1 to include localization in time. Note also that when $\mathcal{B} = I$, this wavelet-based formulation becomes equivalent to the space-time formulation, with the wavelet basis being the specific choice of temporal discretization. In this sense, the use of a wavelet transform is motivated in part by the fact that the wavelet basis aligns with the windowing operator, in the sense that windowing to specific time and/or frequency ranges amounts to choosing a limited set of wavelet basis functions.

3.3 Treatment of temporal domain and boundary effect

In this subsection, we first clarify differences in our temporal discretizations. While both formulations treat time as an explicit coordinate, the construction of $\boldsymbol{D}_t$ differs. In direct space-time resolvent analysis, we construct $\boldsymbol{D}_t$ using a spectral Fourier method (though due to the time-varying mean flow, the Fourier modes do not decouple as in standard resolvent analysis). In contrast, in the wavelet-based formulation, we take $\boldsymbol{D}_t$ to be an explicit differentiation matrix constructed using a first-order finite difference scheme, with Neumann-type boundary conditions in time, that is subsequently discrete wavelet-transformed as described in § 3.2. In both formulations, time is treated as an explicit coordinate on a uniform grid.

In addition, special care is required near the boundaries of the finite time and spatial domains. To mitigate spurious reflections at artificial boundaries, sponge layers have previously been used in global stability analysis [31–33]. Building on this approach and adapting it to the present time-varying framework, we first extend the time domain and apply a sponge region in both space and time. The temporal sponge acts as an artificial boundary condition that allows for robust temporal modes that grow compactly within the physical time domain, while ensuring that the modes decay at the boundaries, which as discussed below are artificially extended.

Furthermore, the spatial sponge allows focus to be directed to the lower boundary, even though the mean shear is small in this region. We note that without the spatial sponge, the modes will typically peak in amplitude near the upper wall, where the global maximum of the mean shear is located.

The time domain is extended to $[-T_{\text{buf}},\ T + T_{\text{buf}}]$, where T is the physical duration and T_{buf} is a buffer length at each end. This yields an extended window of length $T + 2T_{\text{buf}}$, with a step size $\Delta t_{ext} = (T + 2T_{\text{buf}})/N_{t,\text{ext}}$. The subscript "ext" indicates that the temporal domain has been extended. The domain is extended such that the mean velocity profile in the extended regions is constant in time and equal to the profiles at the beginning and end of the simulations. We apply an overlapping sponge function constructed directly in the (y, t) grid [34]. The total sponge field is defined as

$$\boldsymbol{s}(y,t) = \frac{A_{\text{sp}}}{2}\max\left[\tanh\left(\frac{y-\delta_y^{\text{off}}}{\delta_y^{\text{trans}}}\right)+1,\ \tanh\left(\frac{-t+\delta_{t,\text{up}}^{\text{off}}}{\delta_t^{\text{trans}}}\right)+\tanh\left(\frac{t-\delta_{t,\text{down}}^{\text{off}}}{\delta_t^{\text{trans}}}\right)+2\right].$$

where δ_y^{off}, $\delta_{t,\text{up}}^{\text{off}}$, and $\delta_{t,\text{down}}^{\text{off}}$ shift the onset of damping away from the physical boundaries in the wall-normal and temporal directions, respectively, while δ_y^{trans} and δ_t^{trans} control the smoothness of the transition. The sponge amplitude is scaled by $A_{\text{sp}} = 70$. With these parameters, the formulation yields negligible damping over the physical window and ramps smoothly to its maximum in the extended regions and in the upper half of the domain. It therefore forms two symmetric temporal damping layers at the beginning and end of the extended time domain, overlapping the copied initial and final snapshots.

Each temporal sponge rises from zero at the edges of the physical domain and reaches its maximum amplitude A_{sp} near the midpoint of the extended buffer. In the wall-normal direction, the sponge limits the influence of dynamics above a prescribed wall-normal cutoff (here, $y \simeq 1$), ensuring that our analysis focuses on near-wall structures at the bottom wall.

The sponge region acts on both the direct space-time resolvent operator and wavelet-based resolvent operator. The sponge acts as a linear damping that is added to velocity components of the resolvent operator. Letting $\boldsymbol{S}$ denote the reshaped diagonal sponge matrix from $\boldsymbol{s}(y,t)$, which has the same size as the linear operator $\boldsymbol{L}$, the space-time resolvent with this sponge becomes

$$\boldsymbol{\mathcal{H}}_t^{(\mathrm{sp})} = \begin{bmatrix} \boldsymbol{D}_t + \boldsymbol{L} + \boldsymbol{S} & \widehat{\boldsymbol{\nabla}} \\ \widehat{\boldsymbol{\nabla}}^T & 0 \end{bmatrix}^{-1}, \boldsymbol{\mathcal{H}}_w^{(\mathrm{sp})} = \begin{bmatrix} \widetilde{\boldsymbol{D}}_t + \boldsymbol{L} + \boldsymbol{S} & \widehat{\boldsymbol{\nabla}} \\ \widehat{\boldsymbol{\nabla}}^T & 0 \end{bmatrix}^{-1}. \tag{5}$$

Figure 2 illustrates the resulting (y,t)-dependent sponge field $\boldsymbol{s}$ and the physical region (DNS simulation domain) bounded by the vertical lines.Despite the differences in the temporal differentiation operator, we note that the modes grow compactly within the physical time domain and in the spatial region of interest, and are robust between the two resolvent formulations.

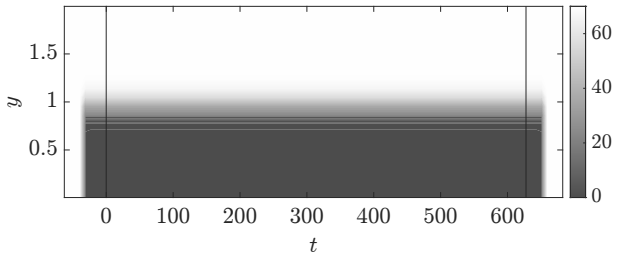

Figure 2: Temporal and spatial sponge enforcing decay near the extended-window boundaries and focusing the analysis on the near-wall region; vertical lines mark the physical interval where DNS data define the base flow. The sponge intensity increase toward white, while the non-sponge region is shown in gray. The total duration of the simulation is $T = 620$ with a temporal buffer region of $T_{\mathrm{buf}} = 63$. Sponge function parameters: $\delta_y^{\mathrm{off}} = -0.0045$, $\delta_y^{\mathrm{trans}} = 0.1$, $\delta_{t,\mathrm{up}}^{\mathrm{off}} = -30$, $\delta_{t,\mathrm{down}}^{\mathrm{off}} = 715.38$, and $\delta_t^{\mathrm{trans}} = 0.5$.

3.4 Resolvent parameters

In both resolvent formulations, a Fourier transform is performed in the homogeneous spatial directions x and z. Hence, a choice of the streamwise and spanwise wavenumber (k_x, k_z) needs to be supplied in order to construct the resolvent operator. To determine an appropriate spatial scale, we use the premultiplied two-dimensional (2D) energy spectra of the streamwise velocity near the bottom wall at various times computed from the DNS ensemble, displayed in Figure 3, which indicate the shortening of streamwise scales and elongation of spanwise scales close to the bottom wall over time. Based on this evolution of high-energy regions across spatial scales, we identify three characteristic streamwise and spanwise wavelengths that represent the dominant energetic structures at different times. To emphasize the streamwise-elongated scales at earlier times, the first length scale is chosen to be $(\lambda_x, \lambda_z)_1 = (6, 1)$, or $(\lambda_x^+, \lambda_z^+)_1 = (345, 57.5)$, where the superscript $^+$ indicates nondimensionalization by the initial friction velocity u_{τ_0} and kinematic viscosity ν. The length scale representative of the flow state at later times is chosen to be $(\lambda_x, \lambda_z)_3 = (1.98, 2.23)$ $((\lambda_x^+, \lambda_z^+)_3 = (114, 128))$ to capture the spanwise elongation over time. An intermediate length scale, $(\lambda_x, \lambda_z)_2 = (4.83, 1.34)$ $((\lambda_x^+, \lambda_z^+)_2 = (278, 77.1))$, is also selected. We note that these scales lie within the energetic scales of the premultiplied 2D energy spectra (see Figure 3); these representatives are streamwise-elongated beyond the peak of the 2D spectra at earlier times and spanwise-elongated at later times to minimize the overlap between length scales.

4 Cause-and-effect analysis

The cause-and-effect mechanisms are quantified through the resolvent forcing and response modes. Cause and effect has been studied through the lens of resolvent analysis in prior work. In Bae *et al.* [35], removal of the principal nonlinear forcing modes at each time step is found to suppress turbulence; Ballouz *et al.* [26, 27] emphasizes the importance of time-localized nonlinearities and their corresponding transient effect via the wavelet-based resolvent forcing and response modes. Central to this interpretation is the

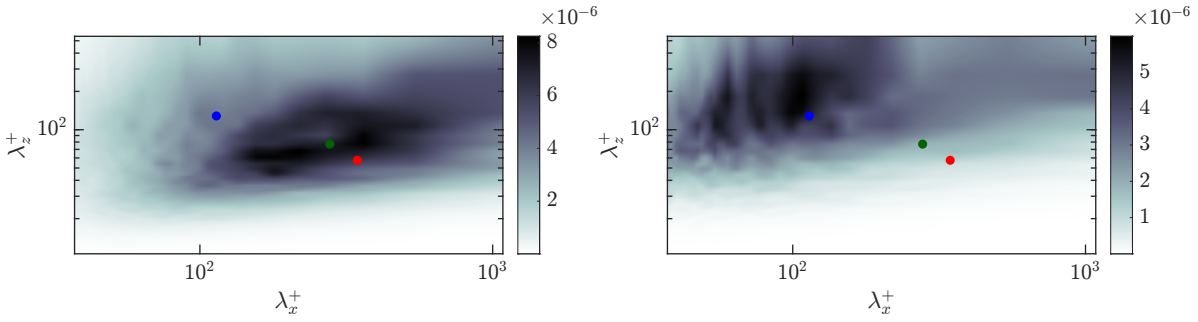

Figure 3: Premultiplied two-dimensional energy spectrum of streamwise velocity fluctuations E_{uu} at $y = 0.0392$ for (a) $t = 0$ and (b) $t = 620$ plotted alongside the representative length scales $(\lambda_x, \lambda_z)_1 = (6, 1)$ $((\lambda_x^+, \lambda_z^+)_3 = (345, 57.5))$ (red), $(\lambda_x, \lambda_z)_2 = (4.83, 1.34)$ $((\lambda_x^+, \lambda_z^+)_2 = (278, 77.1))$ (green), and $(\lambda_x, \lambda_z)_3 = (1.98, 2.23)$ $((\lambda_x^+, \lambda_z^+)_3 = (114, 128))$ (blue).

observation of the resolvent response mode peaking at a later time than that of the forcing. This highlights a distinctive feature of space-time generalizations of resolvent analysis: while there is always a causal relationship between forcing and response in resolvent analysis, this relationship and associated time lags are more apparent when applying space-time resolvent methods where forcing and response modes are localized in time [15]. Hence, in the ensuing analysis, the forcing mode is identified as the "cause", with the response mode representing the "effect", with the intent of studying the cause-and-effect relationship via quantities that effectively describe the linear mechanisms by which the forcing is amplified. More specifically, the time delay between the forcing and response modes can quantify the extent of the causal relation in time. Additionally, for a specified response mode, the corresponding singular value quantifies the relative physical importance of its forcing modes, and therefore quantify the singular value as an amplification factor, representing how strongly the forcing drives the response. These are impacted by the choice of spatial scale and temporal localization used in constructing the resolvent operator, which will be explored in the following subsections.

4.1 Resolvent time delay

The times at which the peak in energy of the forcing and the response modes is observed, $t_{\tilde{\phi}_{\max}}$ and $t_{\tilde{\psi}_{\max}}$, are used to obtain the resolvent time delay $\Delta t_{\text{res}} = t_{\tilde{\psi}_{\max}} - t_{\tilde{\phi}_{\max}}$. This time delay manifests differently across varying streamwise and spanwise spatial scales. Figure 4 shows the resolvent time delay Δt_{res} across different points in the (λ_x, λ_z) parameter space. Notably, the larger streamwise scales are where the largest time delay is observed, whereas the response nearly instantaneously follows the forcing at smaller streamwise scales; additionally, although not shown, the temporal extent of the mode follows the same pattern, where the modes are wider temporally at larger streamwise scales and narrower at smaller streamwise scales. The leading forcing mode at the scale with larger time delays develops from the high-shear temporal region, and its corresponding response extends into the low-shear region. Compared with the 2D energy spectrum at $t = 0$ (see Figure 3), agreement between the energetic spatial scales and the scales illuminating larger time delays is observed, while the energetic scales in the energy spectrum at later times result in modes with smaller temporal extents and time delays.

We next focus on the resolvent modes associated with the spatial scales at earlier and later times, as described in § 3.4. The leading forcing and response modes $\widetilde{\phi_{u_1}}$ and $\widetilde{\psi_{u_1}}$ alongside their y-integrated resolvent kinetic energy $\left[\tilde{\phi}\right] = \int_0^2 |\phi_{u_1}|^2 \, dy$ and $\sigma_1 \left[\tilde{\psi}\right] = \sigma_1 \int_0^2 |\psi_{u_1}|^2 \, dy$, are shown in Figure 5. This representation showcases the temporal extent and kinetic energy peak of the leading forcing and response modes. We note that Δt_{res} is on a similar order for both cases, with $\Delta t_{\text{res}} = 28.7$ for the modes whose length scales are energetic at earlier times, and $\Delta t_{\text{res}} = 22.8$ for the modes whose length scales are energetic at later times. To compare the resolvent time delay with an appropriate time scale from the DNS statistics, we utilize the two-point autocorrelation in streamwise velocity $R_{uu}(y, t, t_{\text{ref}})$, where t_{ref} is a reference time location. R_{uu} is shown for two different reference times in Figure 6. At both $t_{\text{ref}} = 112$ and $t_{\text{ref}} = 557$, R_{uu} peaks sharply at the reference time, with a decay forward and backward from the reference location. A DNS time scale can be extracted via the temporal width of the autocorrelation

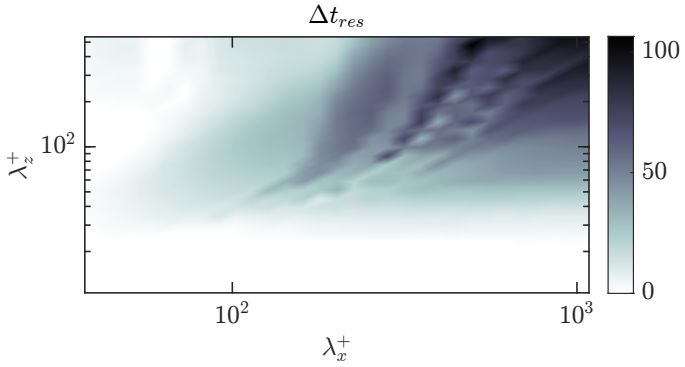

Figure 4: Distribution of resolvent time delay Δt_{res} for different streamwise and spanwise wavelength combinations.

signals at $R_{uu} = 0.5$ [36]; this time scale $t_{uu} = 25.1$ for $t_{\text{ref}} = 112$, and increases slightly at $t_{\text{ref}} = 557$, with $t_{uu} = 31.4$. We note that the resolvent time delays of similar order compared to these DNS scales, indicating that the resolvent operator, representative of a linear amplification process, is able to capture temporal scales similar to those observed in the flow field.

We then apply time windowing to the resolvent operator. Time windows of width $T_{\text{window}} = 53.0$ were centered at a location $t_{0_{\text{window}}}$ corresponding to the peak of the $y-$integrated kinetic energy in the unwindowed modes. Figure 7 shows the time-windowed forcing and response modes for the candidate spatial scales at earlier and later times. We note that the resolvent time delay and amplification, along with the profile of the space-time forcing and response modes, change upon the use of time localization. The time delay $\Delta t_{\text{res}} = 21.3$ at $(\lambda_x, \lambda_z)_1$ is slightly smaller than that of the unwindowed case, and a similar phenomenon occurs at $(\lambda_x, \lambda_z)_3$, with $\Delta t_{\text{res}} = 19.1$. The extent of the windowed response modes in time both decrease. Hence, upon time localization, the growth of response modes is confined due to the restricted forcing window.

4.2 Resolvent amplification

In the ensuing analysis, we compare the singular values of the wavelet-based resolvent analysis before and after time windowing. We consider the leading singular value σ_1; the singular values from the resolvent operator describe the linear kinetic energy amplification of unwindowed or time-windowed forcing perturbations that lead to the response mode. These amplification factors differ as the analysis is confined temporally to the same time window used in Figure 7 (see § 4.1). Namely, the leading amplification of the windowed case $\sigma_{1,w}$ is lower than that of the unwindowed case σ_1; in the high-shear region using scales $(\lambda_x, \lambda_z)_1$, we observe $\sigma_{1,w}/\sigma_1 = 0.753$, and at the low-shear region at scales $(\lambda_x, \lambda_z)_3$, this ratio is slightly higher, with $\sigma_{1,w}/\sigma_1 = 0.859$. This indicates that the optimal forcing outside of the specified window is purposefully excluded upon windowing in time, and any forcing outside of this window (which has a corresponding response) does not provide any contribution to the amplification in this restricted problem.

In addition, we can change the temporal location of the window to observe its effect on σ_1, thereby describing how the forcing drives the response over time at physically relevant temporal regions within the domain. We perform a numerical experiment using windowed wavelet-based resolvent analysis that incorporates time-localized forcing modes. Note that this is in contrast to the analysis in prior sections, which have not imposed such restrictions on the modes. The width of the time window T_{window} is fixed to $T/4$, while the center of the time window $t_{0_{\text{window}}}$ is shifted to different positions in time, and the resolvent operator is constructed separately for each time window prescribed. The leading singular value σ_1 is plotted across varying time windows at the corresponding scales in Figure 8. At $(\lambda_x, \lambda_z)_1$, the resolvent amplification is largest when localizing to initial times, with a subsequent decay as the time window shifts to later times. At $(\lambda_x, \lambda_z)_3$, the amplification is slightly greater when the forcing is restricted to later times. Of particular note is how the change in the amplification is more subtle for the latter spatial scale; further analysis is needed to understand the reason behind this trend.

The change in amplification as the forcing is restricted to earlier and later times, respectively, is also observed across different spatial scales. At each spatial scale, a time-windowed wavelet-based resolvent operator is constructed twice, with time localization in the forcing mode centered at initial and final times; this corresponds to temporal windows of fixed width $T_{\text{window}} = T/4$, but centered at $t_{0_{\text{window}}} = 78.5$ and

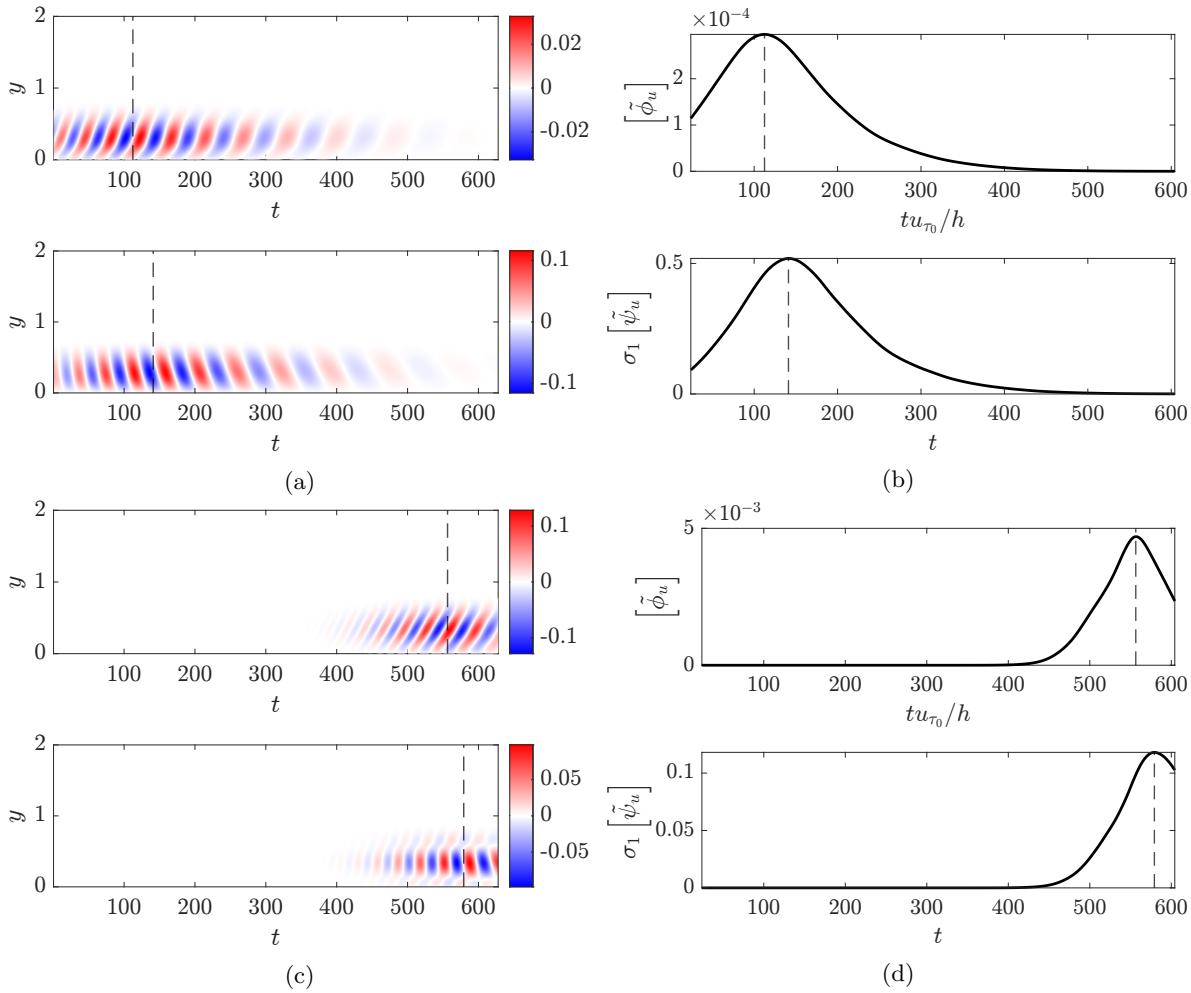

Figure 5: (a, c) Leading wavelet-based resolvent forcing and response modes $\Re(\mathcal{W}^{-1}\widetilde{\phi_{u_1}})$ (top) and $\Re(\mathcal{W}^{-1}\widetilde{\psi_{u_1}})$ (bottom) in the y–t plane at spatial scales (a) $(\lambda_x, \lambda_z)_1$ and (c) $(\lambda_x, \lambda_z)_3$. (b, d) The y-integrated kinetic energy of the forcing (top) and response (bottom) mode at spatial scales (b) $(\lambda_x, \lambda_z)_1$ and (d) $(\lambda_x, \lambda_z)_3$.

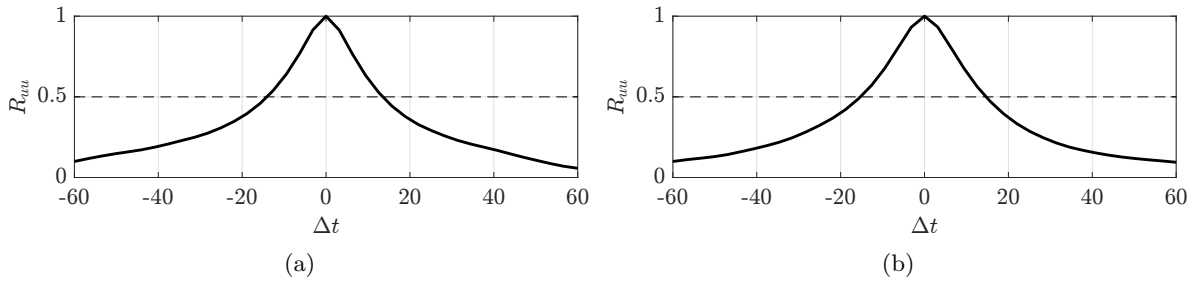

Figure 6: Two-point autocorrelation of streamwise velocity R_{uu}, plotted against temporal shift Δt, centered at times (a) $t_{\text{ref}} = 112$ and (b) $t_{\text{ref}} = 557$, with the dashed lines indicating $R_{uu} = 0.5$.

$t_{0_{\text{window}}} = 550$. The difference between the leading singular values $\Delta\sigma_1$ for both operators across different (λ_x, λ_z) combinations is shown in Figure 9. Similar to Figure 4, the larger streamwise scales capture greater amplification in the resolvent operator windowed to initial times, while the smaller streamwise (and larger spanwise) scales indicate more amplification in the modes windowed to later times. We note that the modes corresponding to $(\lambda_x, \lambda_z)_1$ and $(\lambda_x, \lambda_z)_3$ are representative of the range of amplification

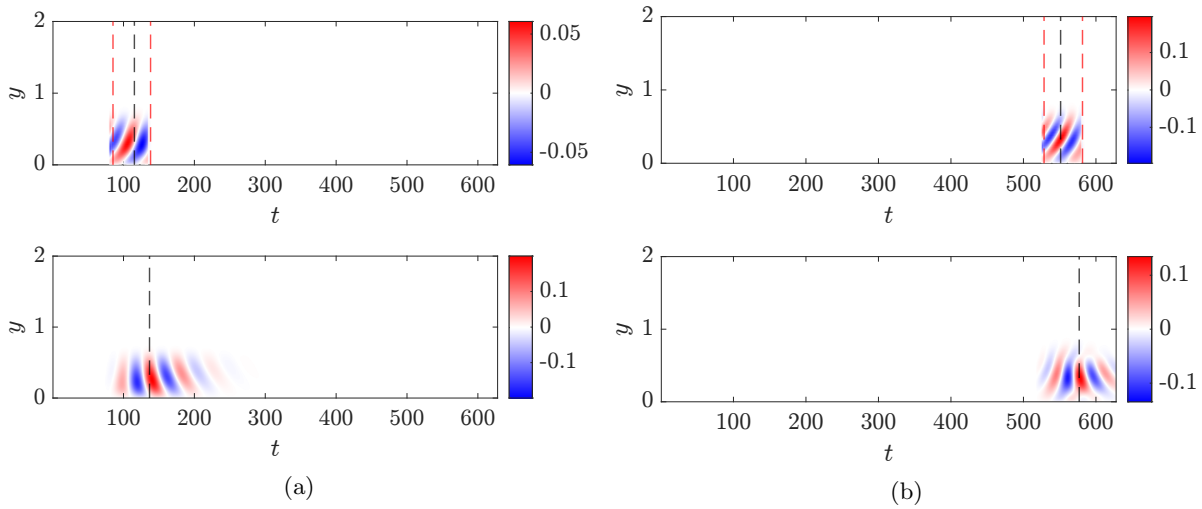

Figure 7: Leading time-windowed wavelet-based resolvent forcing and response modes $\Re(\mathcal{W}^{-1}\widetilde{\phi_{u_1}})$ (top) and $\Re(\mathcal{W}^{-1}\widetilde{\psi_{u_1}})$ (bottom) in the $y-t$ plane at spatial scales (a) $(\lambda_x,\lambda_z)_1$ and (b) $(\lambda_x,\lambda_z)_3$.

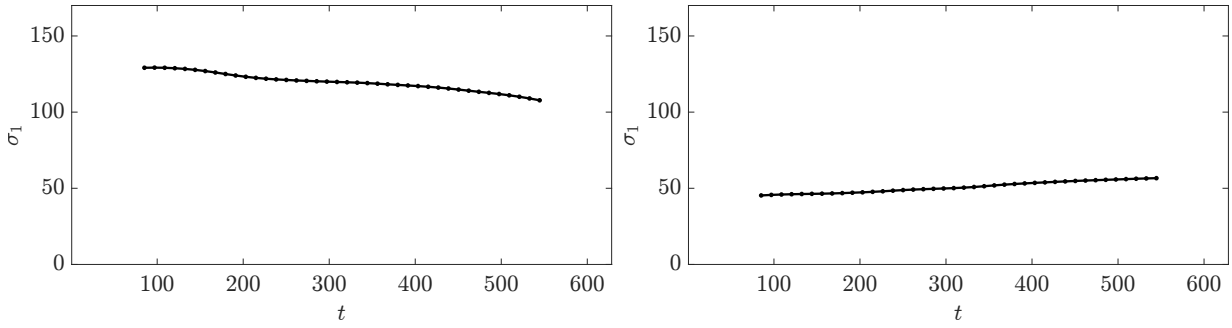

Figure 8: Resolvent amplification σ_1 calculated at time windows centered at different times for spatial scales (a) $(\lambda_x,\lambda_z)_1$ and (b) $(\lambda_x,\lambda_z)_3$ for $T_{\text{window}} = T/4$.

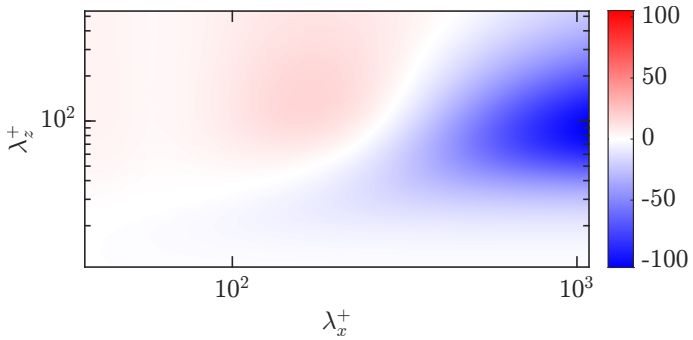

Figure 9: Distribution of the difference in the resolvent amplification $\Delta\sigma_1$ with time windowing at later times ($t_{0_{\text{window}}} = 550$) and at earlier times ($t_{0_{\text{window}}} = 78.5$), for different streamwise and spanwise wavelength combinations.

across windows at the temporal extrema. These trends across spatial scales show agreement with the energetic scales in the energy spectrum (see Figure 3). This indicates that resolvent analysis yields results consistent with the DNS, in terms of the times at which certain spatial scales yield preferential energy amplification.

Hence, via time localization and identification of quantities describing the relationship between forcing and response modes, transient cause-and-effect mechanisms and their importance at different times can be observed. The time delay and amplification both manifest differently at scales whose energy are contained in the high- and low-shear time regions, and time localization can describe the importance of impulse forcing at physically relevant times on the corresponding flow features.

5 Resolvent-based modeling of transient flow separation

In this section, we develop a reduced-order model to represent the dynamics of the turbulent C-P flow using a small number of leading space-time resolvent modes [5, 37]. The reconstruction here is based on a model consisting of the time-varying base flow $U(y,t)$ and three space-time resolvent modes:

$$u(x,y,t) = U(y,t) + \sum_{i=1}^{3} A_i \,\mathrm{Re}\big\{\psi_{u_i}(x,y,t)\big\}, \tag{6}$$

where A_i is the amplitude of mode i, and ψ_{u_i} is the corresponding space-time resolvent mode in the streamwise direction. Each mode represents the leading response at a specific streamwise-spanwise scale selected from the candidate scales identified in § 3.4. To avoid ambiguity, the three modes are referred to as long-streamwise/narrow-spanwise, intermediate, and short-streamwise/wide-spanwise modes.

5.1 Positive flow fraction

To quantitatively characterize the presence of forward-moving fluid at different wall-normal locations and times, we define the positive flow fraction (PFF). This quantity represents the probability that the streamwise velocity u is positive at a given wall-normal location y and time t. The PFF is mathematically defined as

$$\mathrm{PFF}_{\mathrm{DNS}}(y,t) = P\{u(x,y,z,t) > 0\}, \tag{7}$$

where $P\{\cdot\}$ denotes the probability of positive streamwise flow over the (x,z) plane at fixed y and t. In other words, for each y, we examine how often the local streamwise velocity is aligned with the bulk flow direction. The value of $\mathrm{PFF}_{\mathrm{DNS}}(y,t)$ varies between 0 and 1. $\mathrm{PFF}_{\mathrm{DNS}}(y,t) = 1$ indicates that at this wall-normal position, the flow is entirely forward-moving. $\mathrm{PFF}_{\mathrm{DNS}}(y,t) = 0$ indicates complete flow reversal at that location. Intermediate values correspond to mixed states, where both forward and backward motions coexist. Sometimes, it is useful to evaluate the PFF at a specific distance from the wall, $y = y_0$. In this case, the positive flow fraction simplifies to a time-dependent scalar,

$$\mathrm{PFF}_{\mathrm{DNS}}(y_0,t) = P\{u(x,y_0,z,t) > 0\}, \tag{8}$$

where y_0 is fixed and the probability is still taken over the horizontal (x,z) plane. This scalar function $\mathrm{PFF}_{\mathrm{DNS}}(y_0,t)$ is particularly useful for tracking flow separation and reattachment dynamics near the wall. By comparing $\mathrm{PFF}_{\mathrm{DNS}}(y_0,t)$ computed from the full DNS data and from the reduced-order mode built with the resolvent modes, we can quantitatively assess how well the resolvent model captures the temporal behavior of separation events. Figure 10 shows the time evolution of $\mathrm{PFF}_{\mathrm{DNS}}$ evaluated at $y = 0.04$, with the chosen parameters in equation (6)

$$\begin{aligned} A_1(\lambda_x = 6, \lambda_z = 1) &= 1.5, \\ A_2(\lambda_x = 4.83, \lambda_z = 1.34) &= 5, \\ A_3(\lambda_x = 1.98, \lambda_z = 2.23) &= 20. \end{aligned}$$

The three modes are designed to represent different dynamical features of the flow. In this case, we have prior knowledge of the DNS data, so we manually tune the coefficients A_i to match the DNS results. However, this model also has the potential for predictive applications. A direction for future work is to develop a framework that does not rely on prior knowledge of the DNS data. The long-streamwise/narrow-spanwise mode at $(\lambda_x, \lambda_z)_1$ captures the slowly varying, large structures associated with near-wall separation. The intermediate scales mode at $(\lambda_x, \lambda_z)_2$ captures medium-sized flow features. Finally, the short-streamwise/wide-spanwise mode at $(\lambda_x, \lambda_z)_3$ introduces smaller-scale oscillations in the streamwise direction that are representative of higher-frequency turbulent motions. The combined effect of these three modes, together with the time-varying base flow, allows the model to replicate the essential temporal behavior of the PFF observed in DNS. In Figure 10, we show that the 3-mode model can accurately capture the time evolution of PFF at a location near the lower wall. Initially, the PFF

remains close to 1, indicating predominantly forward flow across the entire domain. As time evolves, the inclusion of the three resolvent modes causes localized backflow regions to develop, and the PFF decreases monotonically. Overall, the comparison illustrates that a superposition of a small number of physically interpretable space-time resolvent modes can provide a reduced-order description of the temporal dynamics of near-wall flow reversal events.

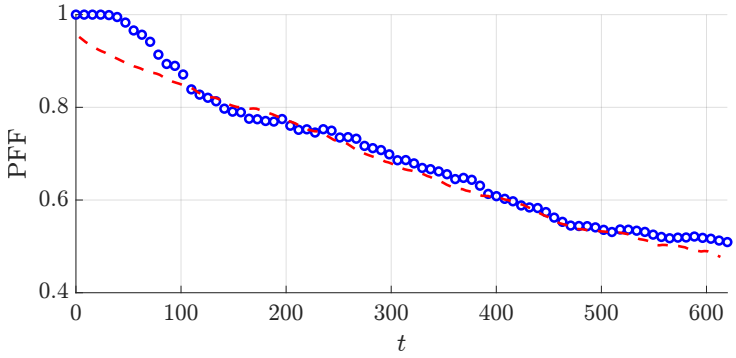

Figure 10: Positive flow fraction PFF$(y = 0.04, t)$ from the resolvent model compared with DNS statistics. Blue circles represent the model prediction, and the red dashed line shows the DNS data.

5.2 Flow visualization

With a model that accurately captures the positive flow fraction at $y = 0.04$, we can visualize it by reconstructing the flow field in the (x, z) planes. This allows us to examine the dominant low-order structures represented by our model within the flow field. This reduced-order representation is then visualized by plotting the (y, t) plane direct space-time resolvent modes and the (x, z) plane streamwise velocity field. The former emphasizes temporal modulation and wall-normal dynamics, while the latter provides an intuitive physical interpretation of how the structures evolve in space.

Using the same coefficients A_i as before, Figure 11 illustrates the components of the proposed model. Row i shows the superposition of the base flow and the leading resolvent response mode ψ_{u_1} at the corresponding length scale $(\lambda_x, \lambda_z)_i$ on the y–t plane, with three representative time instants, t_1, t_2, and t_3, indicated. The three components differ in the choice of length scales and the coefficient, represented by different pairs of streamwise and spanwise wavelengths which serve as parameters to the resolvent formulation. It is clearly observed that different choices of length scales result in modes localized at early, intermediate, and later times. Although the intensity varies due to the differences in coefficients, the key point is that combining a few selected length scales provides a time-resolved model that captures the essential DNS statistics over the entire physical domain, using only a simple model with three representative scales.

At a fixed wall-normal location, $y = 0.04$, figure 12 shows the reconstructed flow field using a single mode (and the mean) in the x–z plane. Once again, differences in intensity can be observed at early, intermediate, and later times. Moreover, the x–z visualization highlights more clearly how the streamwise structures vary under different choices of characteristic length scales. The first wavelength pair, $(\lambda_x, \lambda_z)_1$, exhibits a longer streamwise structure that appears earlier in time. In contrast, the last wavelength pair, $(\lambda_x, \lambda_z)_3$, produces structures that emerge later and are shorter in the streamwise direction. This observation is further supported by Figure 13, which shows a comparison with the corresponding DNS snapshots.

Figure 13 presents the complete three-mode model on different planes, which consists of the mean flow combined with the three selected direct space-time resolvent modes. At the initial time t_1, both the model and the DNS exhibit elongated flow structures in the streamwise direction on the $x - z$ plane. As the time progresses to t_2 and t_3, a similar trend can be observed in both the model and the DNS: the streamwise structures on the x–z plane at $y = 0.04$ become increasingly less pronounced over time. It is also important to note that the model reconstruction is based on only three modes. As a result, while the temporal evolution and the large-scale organization of near-wall structures are approximated, the finer details of turbulent flow cannot be fully captured. However, the agreement between the model predictions and the DNS snapshots further supports that the proposed PFF acts as an effective indicator of near-wall dynamics. Specifically, when the model successfully captures the temporal evolution of the

near-wall PFF consistent with DNS, the corresponding spatial variations in the flow field are expected to exhibit similar trends.

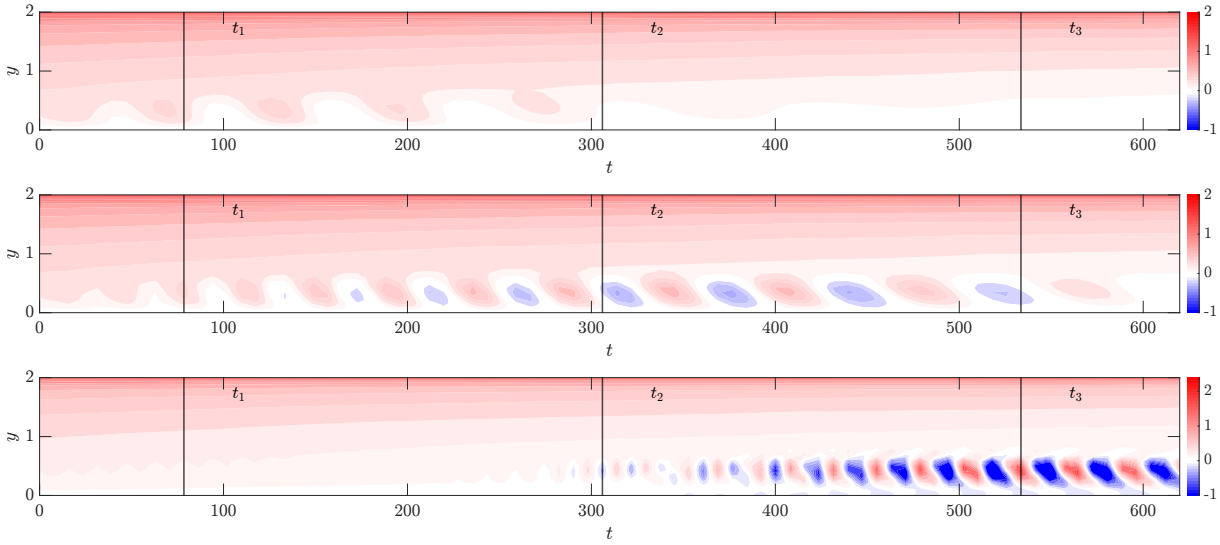

Figure 11: Instantaneous streamwise velocity from the model combining only mean flow and the response modes at a single length scales, visualized on the (y, t) plane. Each row corresponds to a representative wavelength pair $(\lambda_x, \lambda_z)_1$, $(\lambda_x, \lambda_z)_2$, and $(\lambda_x, \lambda_z)_3$. Vertical lines denote three selected time instants t_1, t_2, and t_3.

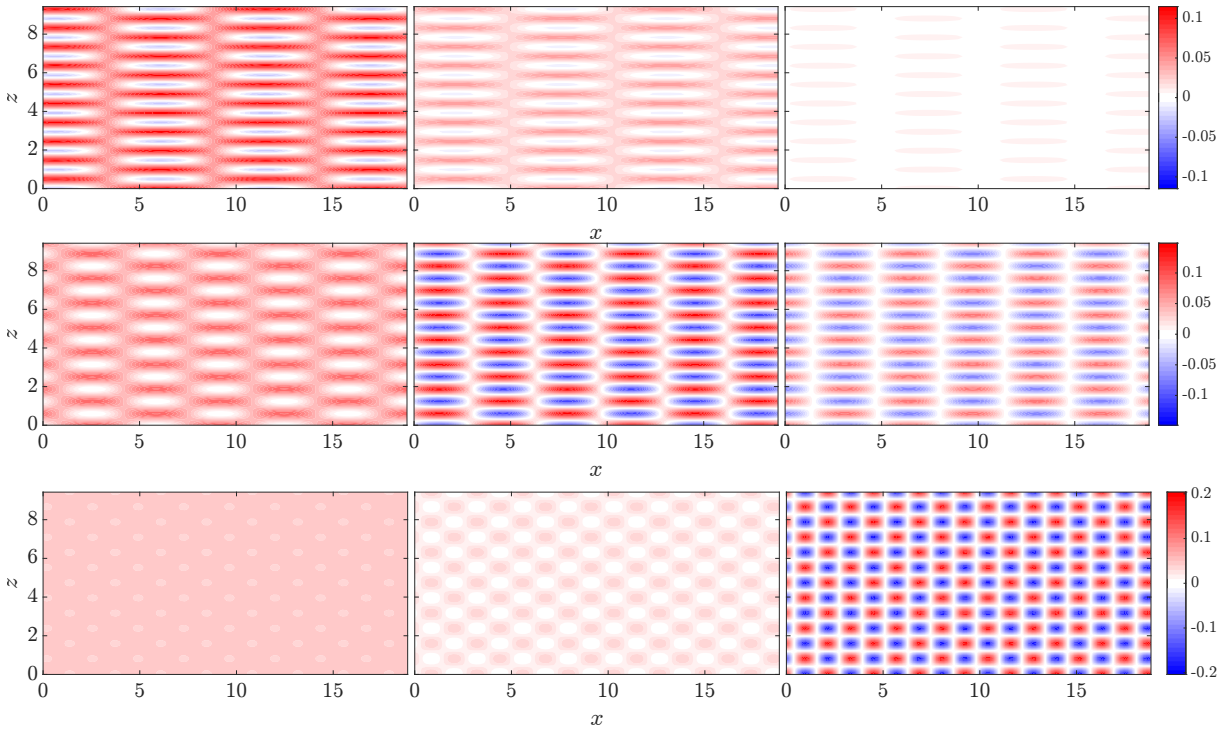

Figure 12: Instantaneous streamwise velocity from the model consisting only mean flow and the response modes at a single length scales, visualized on the (x, z) plane. Each row corresponds to a different length scale $(\lambda_x, \lambda_z)_1$, $(\lambda_x, \lambda_z)_2$, and $(\lambda_x, \lambda_z)_3$, while the columns (from left to right) represent the temporal evolution at t_1, t_2, and t_3, respectively, consistent with Figure 11.

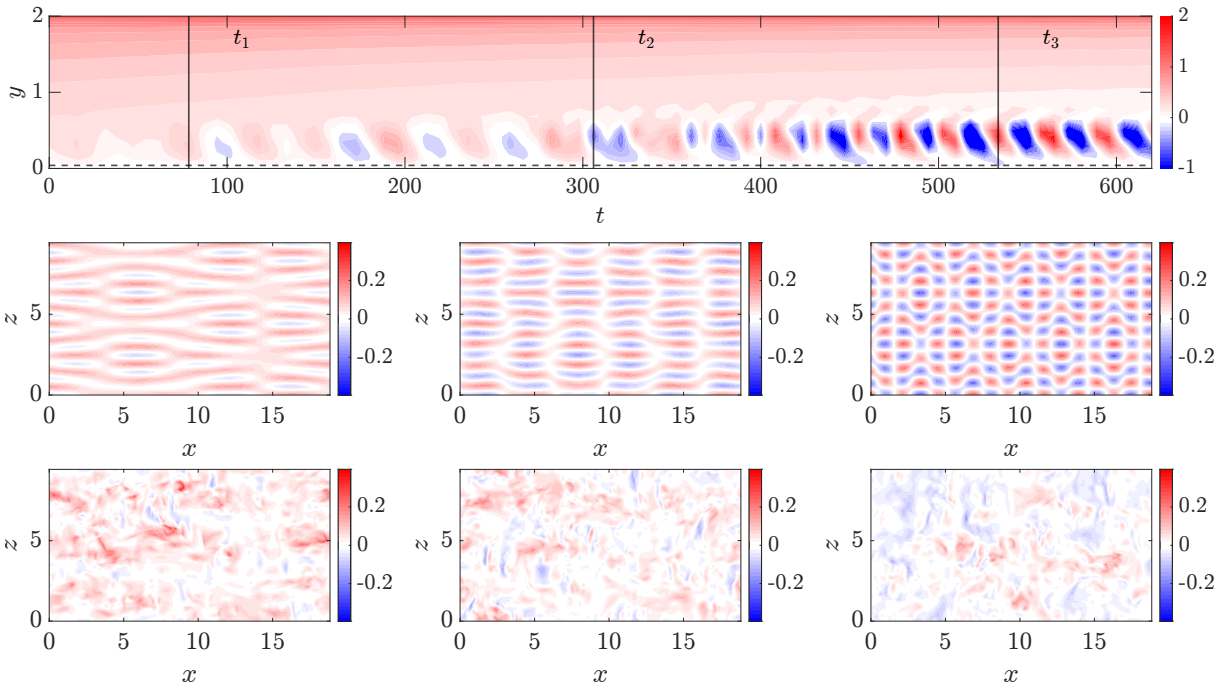

Figure 13: Comparison between the complete three-mode model and DNS snapshots. The top panel shows the complete three-mode model on the y–t plane, with three time instants indicated. The left column presents the model on the x–y plane at these corresponding times, the middle column shows the x–z plane, and the right column displays the corresponding DNS snapshots.

6 Conclusion

Unlike traditional resolvent analysis, our space-time resolvent frameworks allow for an arbitrarily time-varying base flow. Consequently, our analysis emphasizes the transient temporal evolution rather than assuming statistical stationarity.

Our first objective is to examine whether a cause-and-effect relationship exists in the time domain. Due to the resolvent forcing and response modes illuminating a causal relationship, we can define the resolvent time delay and amplification both as means by which the forcing and response (i.e. cause and effect) are linked. Using the wavelet-based resolvent, we can effectively apply temporal windowing to identify which length scales exhibit more pronounced time delays. The amplification and time delay differ upon time localization, but the trends in the response modes given an impulse forcing indicate that even though there are contributions in the forcing/response pairs that are excluded via time windowing, the effect of flow perturbations earlier in time are observable and comparable with the unwindowed case. In future studies, it may be interesting to further investigate the mode shapes via the mode tilt angles and frequency content and connect them to relevant DNS quantities.

Additionally, to construct a reduced-order model more intuitively, we employ the direct space-time resolvent, in which the temporal differential operator is explicitly formulated. By combining the mean flow with only three leading resolvent modes at distinct scales, we reconstruct a low-dimensional model that successfully captures the positive flow fraction (PFF) near the lower wall. This quantity serves as an indicator of reversal flow or flow separation in the near-wall region.

Furthermore, visualization of the reconstructed flow field in the x–z plane reveals that the model reproduces the characteristic flow evolution observed in the DNS data, namely, the gradual shortening of streamwise structures over time and their transition into dominant spanwise structures. This confirms that the proposed model not only captures key temporal dynamics but also reflects the underlying structural transformation of the turbulent flow.

7 Acknowledgments

This work was supported by the European Research Council under the Caust grant ERC-AdG-101018287 and the Air Force Office of Scientific Research under grant number FA9550-22-1-0109.

References

[1] Yeh C A and Taira K 2019 *J. Fluid Mech.* **867** 572–610 ISSN 0022-1120, 1469-7645
[2] Jones A R, Cetiner O and Smith M J 2022 *Annual Review of Fluid Mechanics* **54** 469–493 ISSN 0066-4189, 1545-4479
[3] Wu W, Meneveau C and Mittal R 2020 *J. Fluid Mech.* **883** A45 ISSN 0022-1120, 1469-7645
[4] Yeh C A, Benton S I, Taira K and Garmann D J 2020 *Phys. Rev. Fluids* **5** 083906 ISSN 2469-990X
[5] McKeon B J and Sharma A S 2010 *J. Fluid Mech.* **658** 336–382 ISSN 0022-1120, 1469-7645
[6] Moarref R, Sharma A S, Tropp J A and McKeon B J 2013 *J. Fluid Mech.* **734** 275–316 ISSN 0022-1120, 1469-7645
[7] Soria J, Matas A, Liu K, Gomez S R, Jaroslawski T and McKeon B J 2024 Biglobal resolvent analysis of a self-similar adverse pressure gradient turbulent boundary layer at the verge of separation *Proceedings of the 2024 Summer Program, Center for Turbulence Research*
[8] Ribeiro J H M and Taira K 2024 *J. Fluid Mech.* **995** A13 ISSN 0022-1120, 1469-7645
[9] Lenaers P, Li Q, Brethouwer G, Schlatter P and Örlü R 2012 *Physics of Fluids* **24** 035110 ISSN 1070-6631, 1089-7666
[10] Vinuesa R, Örlü R and Schlatter P 2017 *J. Turbul.* **18** 170–185 ISSN null
[11] Parthasarathy A and Saxton-Fox T 2025 *Journal of Fluid Mechanics* **1010** A61
[12] Pirozzoli S, Bernardini M and Orlandi P 2011 *J. Fluid Mech.* **680** 534–563 ISSN 0022-1120, 1469-7645
[13] Samson A, Naicker K and Diwan S S 2021 *Physics of Fluids* **33** 094106 ISSN 1070-6631
[14] Lopez-Doriga B, Ballouz E, Bae H J and Dawson S T M 2024 *J. Fluid Mech.* **999** A87 ISSN 0022-1120, 1469-7645
[15] Ballouz E, Lopez-Doriga B, Dawson S T M and Bae H J 2024 *J. Fluid Mech.* **999** A53 ISSN 0022-1120, 1469-7645
[16] Cheng W, Pullin D, Samtaney R and Luo X 2023 *J. Fluid Mech.* **955** A4 ISSN 0022-1120, 1469-7645
[17] Choi Y K, Lee J H and Hwang J 2021 *Int. J. Heat Fluid Flow* **90** 108836 ISSN 0142727X
[18] Wu Z 2021 *The Study of Coherent Structures in Adverse Pressure Gradient Turbulent Couette-Poiseuille Flows with Zero Mean Skin Friction* Ph.D. thesis Monash University
[19] Chong M S, Monty J P and Marusic I 2011 The Topology of Surface Skinfriction and Vorticity Fields in Wall-bounded Flows *Proceeding of Seventh International Symposium on Turbulence and Shear Flow Phenomena* (Ottawa Convention Centre, Ottawa, Canada: Begellhouse) pp 1–6
[20] Cardesa J I, Monty J P, Soria J and Chong M S 2019 *Journal of Fluid Mechanics* **880** R3 ISSN 0022-1120, 1469-7645
[21] Willert C, Soria J, Cuvier C, Foucaut J M and Laval J P 2018 Flow Reversal in Turbulent Boundary Layers with Varying Pressure Gradients (Lisbon, Portugal)
[22] Orlandi P and Moreau R (eds) 2000 *Fluid Flow Phenomena: A Numerical Toolkit* (*Fluid Mechanics and Its Applications* vol 55) (Dordrecht: Springer Netherlands) ISBN 978-1-4020-0389-9 978-94-011-4281-6
[23] Wray A 1991 *NASA Ames Research Center*
[24] Kim J and Moin P 1985 *Journal of Computational Physics* **59** 308–323 ISSN 00219991
[25] Gomez S R and Jaroslawski T 2025 *arXiv preprint arXiv:2511.00258*
[26] Ballouz E, Dawson S T M and Bae H J 2024 *J. Phys.: Conf. Ser.* **2753** 012002 ISSN 1742-6588, 1742-6596
[27] Ballouz E, Dawson S T M and Bae H J 2025 *J. Fluid Mech.* **1016** A19 ISSN 0022-1120, 1469-7645
[28] Daubechies I 2006 *Ten lectures on wavelets* 9th ed (*Regional conference series in applied mathematics* no 61) (Philadelphia, Pa: Society for Industrial and Applied Mathematics) ISBN 978-0-89871-274-2
[29] Mallat S 2009 *A Wavelet Tour of Signal Processing* (Elsevier) ISBN 978-0-12-374370-1
[30] Najmi A H 2012 *Wavelets: A Concise Guide* (Johns Hopkins University Press) ISBN 978-1-4214-0496-7 978-1-4214-0495-0 978-1-4214-0559-9
[31] Ran W, Zare A, Nichols J W and Jovanovic M R 2017 The effect of sponge layers on global stability analysis of Blasius boundary layer flow *47th AIAA Fluid Dynamics Conference* (Denver, Colorado: American Institute of Aeronautics and Astronautics) ISBN 978-1-62410-500-5
[32] Mani A 2012 *Journal of Computational Physics* **231** 704–716 ISSN 0021-9991
[33] Colonius T 2004 *Annual Review of Fluid Mechanics* **36** 315–345 ISSN 1545-4479
[34] Martini E and Schmidt O 2024 *Theoretical and Computational Fluid Dynamics* **38** 665–685 ISSN 1432-2250
[35] Bae H J, Lozano-Durán A and McKeon B J 2021 *J. Fluid Mech.* **914** A3 ISSN 0022-1120, 1469-7645
[36] Jiménez J 2015 *Physics of Fluids* **27** 065102 ISSN 1070-6631, 1089-7666
[37] Sharma A S and McKeon B J 2013 *J. Fluid Mech.* **728** 196–238